Journal of Manufacturing Processes 69 (2021) 173–180

Contents lists available at ScienceDirect

Journal of Manufacturing Processes

journal homepage: www.elsevier.com/locate/manpro

Electrowetting-assisted direct ink writing for low-viscosity liquids

Yizhou Jiang, Xinnian Wang, Jevon Plog, Alexander L. Yarin *, Yayue Pan *

Department of Mechanical and Industrial Engineering, University of Illinois at Chicago, 842 W. Taylor St., Chicago, IL 60607, United States of America

ARTICLE INFO

Keywords:
Direct ink writing
Electrowetting
Printing geometry modeling

ABSTRACT

In conventional direct ink writing (DIW) process, low-viscosity liquids are usually nonprintable, which greatly limits the choices of inks and the potential applications of DIW. To address this challenge, the present work reports a novel electric-field-assisted method to enable DIW of low-viscosity liquids. An external electric field is applied between the dispensing nozzle and the substrate, to vertically pull the printed filament for decreasing the internal pressure along the printing direction. Our proposed method overcomes the common capillary instability characteristic of continuous extrusion of low-viscosity materials. Compared with conventional approaches, the electric-field-assisted DIW process significantly widens the available range of process parameters, increases the throughput by over 150%, and improves the printing accuracy by more than four-fold. These findings indicate an innovative approach for the fabrication of next-generation functional devices using low-viscosity liquids, which used to be difficult or even impossible to print.

1. Introduction

Direct ink writing (DIW), as a versatile additive manufacturing (AM) technique, has been recently demonstrated in numerous fields, including soft robotics, wearable electronics, artificial organs, and high-performance structural composites [1–5]. Compared with other AM approaches, the primary strength of DIW is the diversity of the printable materials. Many liquids, such as functional polymer solutions, liquid metals, conductive composites, and living cells have been utilized as feedstock to print complicated features and three-dimensional structures, promoting the manufacturing of advanced structures using innovative materials [6–9].

A typical DIW system consists of a building platform, computer-controlled mechanical stages, and a nozzle-based ink deposition apparatus [10]. The liquid ink is directly extruded from the nozzle by a pumping device onto the building platform in a filament-by-filament way. In terms of the liquid inks used in DIW, two rheological properties are preferred, namely the shearing-thinning behavior and the viscoelastic behavior [11,12]. The shear-thinning behavior ensures a relatively low pumping pressure when extruding the liquid ink through the nozzle, which effectively prevents nozzle clogging and fracture. On the other hand, the viscoelastic behavior assures a high shape-stability of the printed filaments, which is essential for the printed geometry accuracy. In general, such viscoelastic properties need to be confirmed by moduli (including storage modulus and loss modulus) characterization. Ideally, the printable ink should behave liquid-like when extrusion (at high shear-rate range, storage modulus $<$ loss modulus) and solid-like (at low shear-rate range, storage modulus $>$ loss modulus) after extrusion and seating on the printing substrate [13,14].

However, not many materials exhibit such rheological behavior. Liquids with an apparent viscosity less than 10^{-1} Pa s at zero shear-rate that are usually printable using inkjet printing methods, have been well investigated [15], and are not in focus in the present study. In the DIW process, non-viscoelastic liquids with an apparent viscosity in the 10^{-1} to 10^{2} Pa s range usually suffer from filament shape instability, such as the commonly used solvents, oils, and conducting polymers, which are in focus in this study. This category of liquids reveals tremendous printing difficulties due to its inherent inappropriate rheology [13]. The printed geometry of such materials usually suffers from various instabilities, causing critical geometrical defects, including inconsistent filaments and bulges. To understand the nature of such instabilities, Friedrich et al. derived an analytical model accounting for the influence of the extrusion flow rate, printing speed, and the ink contact angles on the printed filament's shape stability, reporting numerous drawbacks existing in the current DIW processes for printing low-viscosity liquids [13].

To increase the diversity of the printable materials in DIW by enabling low-viscosity material printing, many novel methods have been recently reported. For example, Skylar-Scott et al. designed a laser-assisted DIW process to print freestanding 3D metal structures with

* Corresponding authors.
E-mail addresses: ayarin@uic.edu (A.L. Yarin), yayuepan@uic.edu (Y. Pan).

https://doi.org/10.1016/j.jmapro.2021.07.028
Received 5 December 2020; Received in revised form 11 June 2021; Accepted 10 July 2021
Available online 30 July 2021

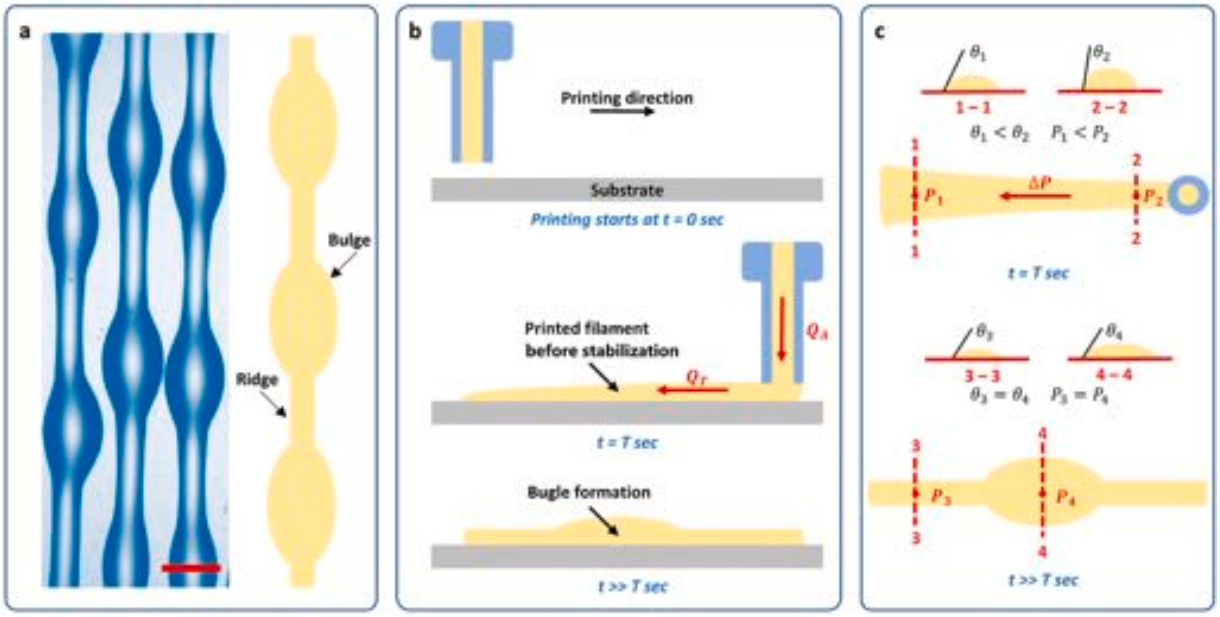

Fig. 1. Analysis of bulge formation. (a) Unstable filaments of 5 wt% PVA aqueous solution printed on polyimide by DIW. Bulge and ridge indicated, scale bar is 1 mm. (b) Illustration of bulge formation, side view. (c) Illustration of bulge formation, top view.

relatively high conductivity using concentrated silver nanoparticle composites [14]. By focused infrared laser annealing, the thin Ga-In alloy-based inks can be rapidly solidified to compensate for the structural instabilities. Kim et al. used a temperature-controlled platform to instantly cure the low-viscosity elastomer-based ink to fabricate programmable soft structures [2]. These methods are effective for specific stimuli-curable low-viscosity materials. However, printing a broad type of non-curable low-viscosity liquids in DIW is still a grand and ongoing challenge. Thickening agents are commonly used as additives to change the rheology of low viscosity liquids to improve their printability. Nevertheless, the additives inevitably degrade the characteristics of the original materials and are undesirable for some applications [16].

Against this background, to overcome the current limitation in DIW of low-viscosity liquids, we introduce here a novel electric-field-assisted DIW method. By modifying the substrate's wetting properties using an applied electric field between the dispensing nozzle and the building platform, the deposit instability can be significantly diminished, leading to a highly improved geometrical accuracy in the DIW of low-viscosity materials. The rest of the article is organized as follows. Section 2 investigates the electric-field-assisted DIW process to reveal the printed liquid behavior under an applied electric field. Section 3 presents the ink preparation and characterization, hardware setup, and the fabrication process. Section 4.1 discusses the influence of the electric field strength on the working range of DIW process parameter settings. Section 4.2 analyzes the printing quality of the proposed electric-field-assisted method statistically using an image processing approach. Conclusions and the outlook are summarized in the end.

2. Methodologies

In extrusion-based additive manufacturing processes, shape instabilities in printed filaments are common issues that can significantly degrade the geometrical accuracy. A printed filament may become unstable by forming a series of liquid bulges connected by a ridge of liquid. Fig. 1a shows several unstable filaments. They were the filaments printed through a 23-gauge nozzle onto a polyimide substrate at the 9 mm/s printing speed under the 3 mm^3/s extrusion rate. To explain the formation of such instabilities, we first identify the two types of flow conditions that exist in the DIW process, namely the applied flow Q_A and transported flow Q_T [17,18]. Herein, Q_A is defined as the rate of liquid exiting from the dispensing nozzle, which is directly controlled by the pumping system. On the other hand, after the filament was printed onto the substrate, but before stabilization, there is a temporary transported flow Q_T caused by the liquid instability. The transported flow is induced by the internal pressure ΔP from the deviations in dynamic contact angles of the continuous filament. For example, as shown in Fig. 1b and c, we assume that the printing direction is from location 1 to location 2, and printing starts at $t = 0$ and ends at $t = T$. Under these conditions, the contact angles at locations 1 and 2 are denoted as θ_1 and θ_2 with internal pressure P_1 and P_2, respectively. Similarly to many extrusion-based AM techniques, the typical printing speed in the DIW process is set at less than 20 mm/s to smoothly write the curved features [1]. Also, to avoid filament breakup, the applied flow rate is usually set to a level that enables an extruded filament slightly wider than the nozzle diameter, meaning that the advancing contact angle of the liquid can be reached when the droplet continues to grow after extrusion at a certain location. As the nozzle moves and leaves this location after printing, the droplet starts to settle and eventually stabilizes on the substrate with an equilibrium contact angle. Such a phenomenon can lead to significant differences in the contact angles along the printed filament due to the time delay. Here, when the dispensing nozzle is at location 2 ($t = T$), the real-time contact angle θ_1 is similar to the equilibrium contact angle θ_E due to the settling at location 1 already reached at time T. On the other hand, the real-time θ_2 is closer to the advancing contact angle θ_A due to the lower settling time. Accordingly, the related capillary pressure difference ΔP caused by the time-dependent dynamic contact angles can trigger a formation of a bulge under the following circumstances [17]:

$$KQ_A < Q_T; Q_A = Av \tag{1}$$

where K is a constant that can be experimentally characterized [19], v is the substrate speed, and A is the cross-sectional area of the printed filament. The transported flow rate is based on Duineveld's work [17]:

$$Q_T = \frac{4S\Delta PA^2}{\eta l_r} \tag{2}$$

where S is the cross-section coefficient.

$$S = \frac{\theta_E - sin\theta_E cos\theta_E}{8(sin\theta_E + \theta_E)^2} \tag{3}$$

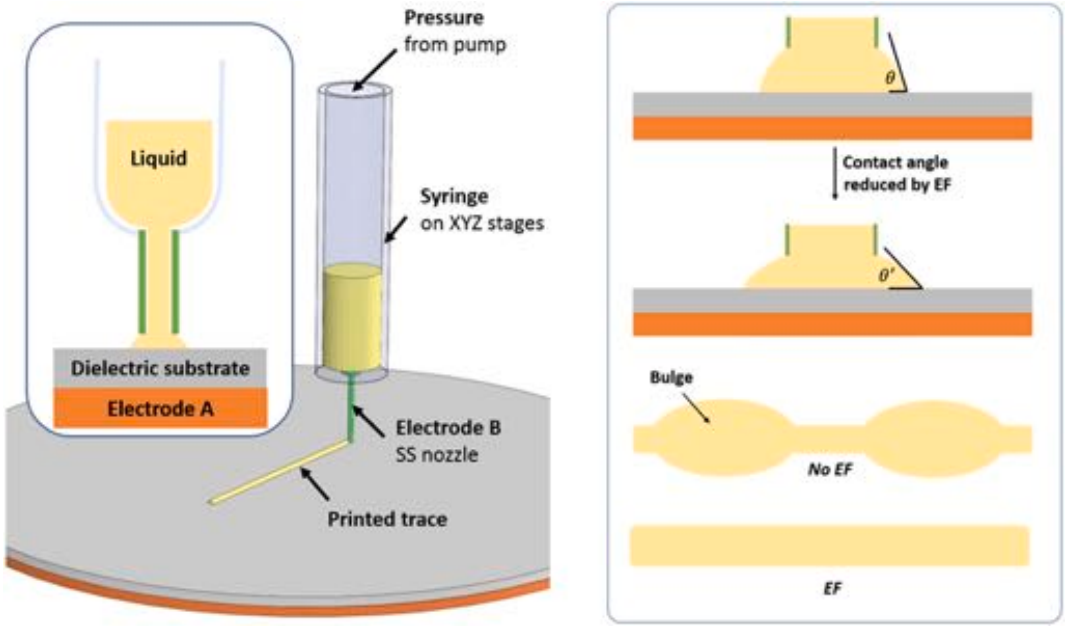

Fig. 2. Electric-field-assisted DIW. (a) Sketch of electric-field-assisted DIW configuration. (b) Illustration of the advancing contact angle affected by EF during printing.

ΔP is the capillary pressure difference between the bulge and the ridge, η is the material apparent viscosity, l_r is the minimum ridge distance. According to Stringer and Derby's work on inkjet printing, l_r is identical to the droplet spacing [18]. Considering the continuous extrusion mechanism of DIW, for ease of calculation, we followed our previous work and set l_r at a relatively small value of 5 μm in this study [19]. The printed filament width W in a typical DIW configuration is:

$$W = 2Q_A^{\frac{1}{2}} v^{-\frac{1}{2}} \left(\frac{\theta_E}{sin^2\theta_E} - \frac{cos\theta_E}{sin\theta_E} \right)^{-\frac{1}{2}} \tag{4}$$

The dynamic pressure in a printed filament, P, with width W and real-time contact angle θ can be approximated as:

$$P = \frac{2\sigma sin\theta}{W} \tag{5}$$

where σ is the surface tension of the liquid.

When t ≫ T, the contact angles along the filament tend to be equal, resulting in a significantly reduced internal pressure between the ridge (locations 3, the contact angle denoted as θ_3 with the capillary pressure P_3) and the bulge (location 4, the contact angle denoted as θ_4 with the capillary pressure P_4) [17]. The printed filament eventually reaches its stable state ($P_3 \approx P_4$) by minimizing the surface energy. The dynamic contact angles during the printing process are characterized as:

$$\theta_E < \theta_3 = \theta_4 < \theta_1 < \theta_2 < \theta_A \tag{6}$$

The upper bound of the internal pressure difference, ΔP, based on Eq. (5):

$$\Delta P = \frac{2\sigma(\sin\theta_A - \sin\theta_E)}{W} \tag{7}$$

By substituting the width W from Eq. (4), the critical substrate speed for bulge-free printing could be calculated:

$$v_{critical} = f(\sigma, \eta, \theta_A, \theta_E, Q_A) = K^{-\frac{2}{3}} \left[\frac{4S\sigma}{\eta l_r} (sin\theta_A - sin\theta_E) \sqrt{\frac{\theta_E}{sin^2\theta_E} - \frac{cos\theta_E}{sin\theta_E}} \right]^{\frac{2}{3}} Q_A^{\frac{1}{3}} \tag{8}$$

Eq. (8) shows that the critical printing speed for bulge-free filament printing is a function of material viscosity, surface tension, equilibrium contact angle, advancing contact angle, and the applied flow rate. This modeling method has been tested and validated using both Newtonian and non-Newtonian liquids in a non-EF configuration [19]. It should be emphasized that Eq. (8) involves an empirical factor K, which should be fitted to the experimental data. In the present work, it is assumed that K does not depend on the electric field. This assumption is supported by the experimental data considered below. In the present work, we extend Eq. (8) to an electric-field-assisted process and investigate the influence of the electric field (EF) on the critical printing speed for defect-free printing. In electrowetting, when an external electric potential is applied between a liquid and solid, the ions in liquid and dipoles in solid can redistribute, resulting in a change of the surface energy at the liquid-solid interface [20,21]. Cations and anions in liquid are almost instantaneously transported towards the parts of the solid surface of the opposite polarity. Accordingly, the liquid becomes polarized, and a bulk Coulomb force pulls the polarized liquid layer near the solute surface towards the latter, which diminishes the contact angle and is termed electrowetting. A wide range of applications, including "lab-on-a-chip" devices, adjustable optical lenses, and innovative electronic displays, have been reported [21].

When applying EF using an electric-field-assisted DIW setup (Fig. 2a), the real-time contact angles of the liquid during printing can be immediately decreased [22–25], which further weakens the influence of the transport flow (Fig. 2b). Under such an electric field, the updated real-time contact angle θ' [26] is described by the Young-Lippmann equation:

$$cos\theta' = cos\theta + \frac{\epsilon V^2}{2\sigma d} \tag{9}$$

where ϵ is the dielectric permittivity of the dielectric substrate, V is the electrical potential difference between electrode A and electrode B (see Fig. 2), d is the thickness of the dielectric substrate.

It should be emphasized that the surface tension of the liquid is also affected by the electric field. Studies have shown that the change in the surface tension under such electric-field configuration is 2% at most [27], which is negligible compared to the changes in the advancing contact angles. To simplify the model, we keep using the non-electric-field-affected surface tension in our study. Taking the effect of

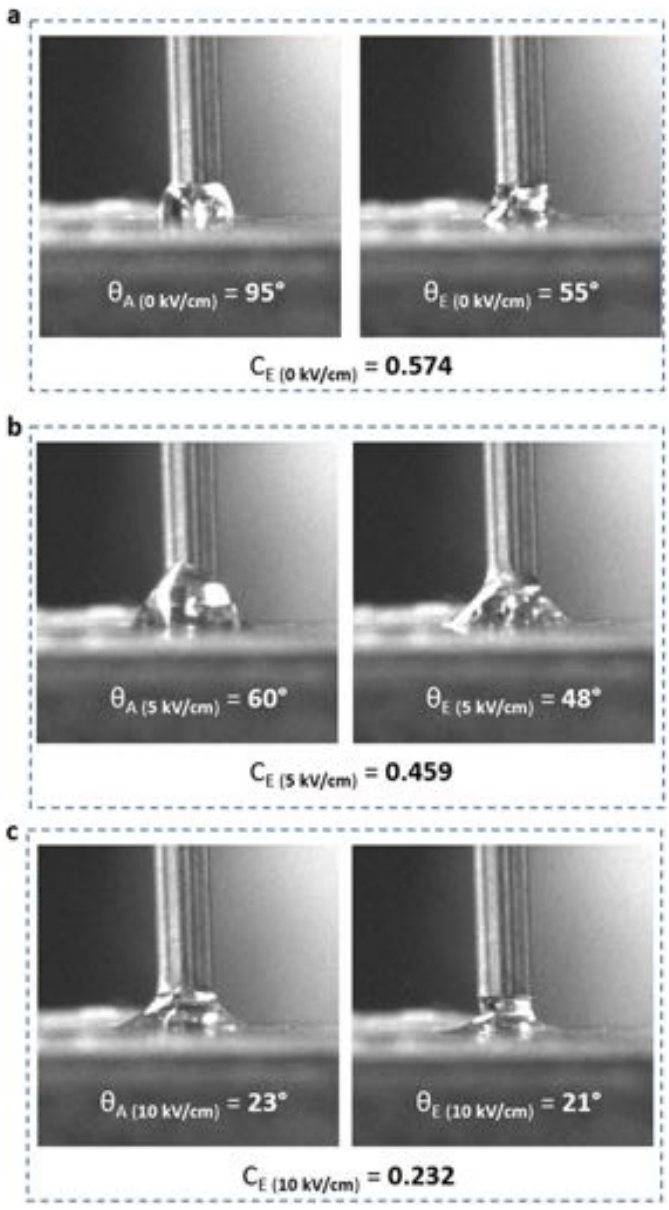

Fig. 3. Average advancing contact angles and equilibrium contact angles. (a) 0 kV/cm. (b) 5 kV/cm. (c) 10 kV/cm.

horizontal component of the electric field into consideration, the critical printing speed for the bulge-free printing is then updated as follows:

$$v'_{critical} = K^{-\frac{2}{3}}\left[\frac{4S\sigma}{\eta l_r}\left(sin\theta'_A - sin\theta'_E\right)\sqrt{\frac{\theta'_E}{sin^2\theta'_E} - \frac{cos\theta'_E}{sin\theta'_E}}\right]^{\frac{2}{3}} Q_A^{\frac{1}{3}} \tag{10}$$

Introduce the lumping coefficient to combine parameters related to the inherent liquid properties as:

$$C_E = K^{-\frac{2}{3}}\left[\frac{4S\sigma}{\eta l_r}\left(sin\theta'_A - sin\theta'_E\right)\sqrt{\frac{\theta'_E}{sin^2\theta'_E} - \frac{cos\theta'_E}{sin\theta'_E}}\right]^{\frac{2}{3}} \tag{11}$$

Then, the updated critical printing speed for DIW can be re-written as:

$$v'_{critical} = C_E Q_A^{\frac{1}{3}} \tag{12}$$

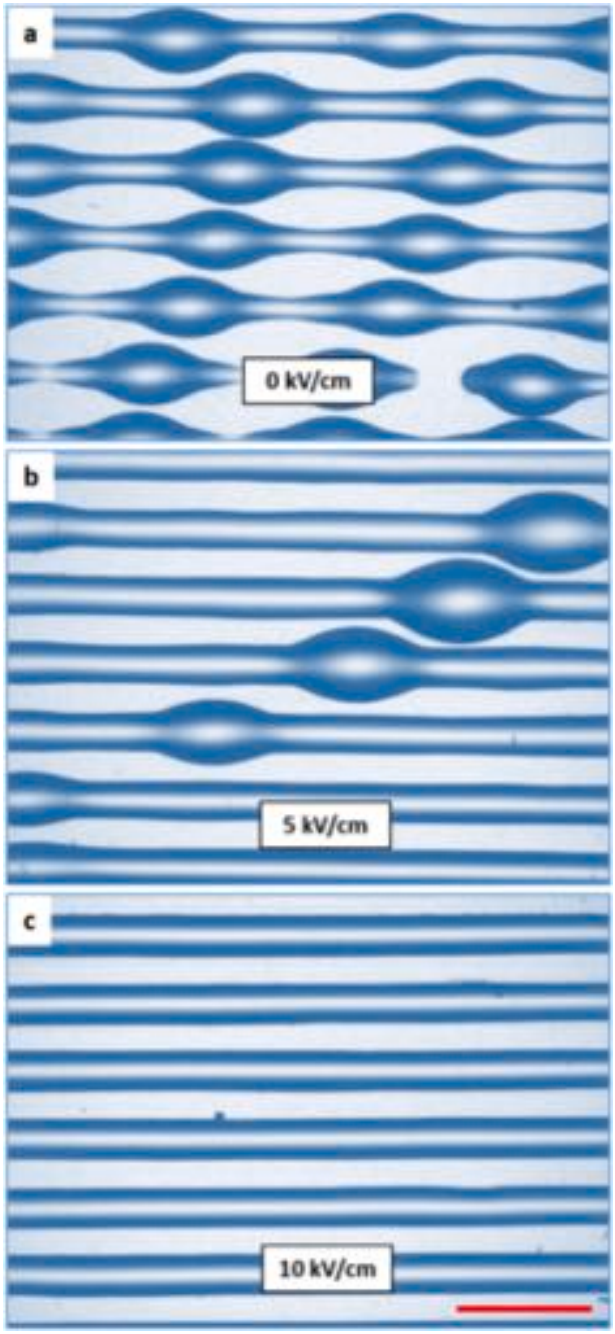

Fig. 4. Printed filaments under different EF strengths. The filaments were printed through 23-gauge dispensing nozzle at the 3 mm^3/s applied flow rate using 5 wt% PVA aqueous solution onto polyimide at 9 mm/s printing speed. Scale bar is 2 mm. (a) 0 kV/cm. (b) 5 kV/cm. (c) 10 kV/cm.

3. Experimental

3.1. Ink preparation

5 wt% aqueous polyvinyl alcohol (PVA) solution was tested as a low-viscosity liquid in this study. It was prepared by adding 5 g PVA powder (Mowiol® 18-88, Sigma-Aldrich, M_w ~130 kDa) to 100 ml deionized water, followed by overnight magnetic stirring at 200 rpm before storing at room temperature.

3.2. Ink characterization

The rheological properties of the 5 wt% PVA solution have been characterized in our previous study [19]. Its apparent viscosity decreased from 13.1 to 1.0 Pa s when the shear-rate increased from 0.1 to 1.0 s^{-1}, indicating that the shear-thinning behavior is relatively strong. The K value of the ink has been characterized to be 3.67 in our previous study [19].

3.3. Electric-field-assisted DIW system

The DIW system used in the study was developed by integrating a customized 60-Watt high-voltage power source into a dispensing robot (E3V, Nordson EFD). The power source's anode was connected to the stainless-steel dispensing nozzle (0.48 mm inner diameter). Its cathode was connected to a thin copper film covered by 0.3 mm thick polyimide (the surface energy: 50 mJ/m^2) as the dielectric substrate on a moving platform. The standoff distance between the dispensing nozzle and the substrate was adjusted to be 0.5 mm. The extrusion pressure was due to a pumping system (Ultimus II, Nordson EFD). The platform temperature during the DIW process was elevated to 75 °C to solidify the PVA solution rapidly. Accordingly, the printing process was implemented by extruding the prepared PVA solution in a filament-by-filament way. The DIW system is also equipped with a CCD camera (Point Grey Research Inc., CMLN-13S2M-CS) to characterize the dynamic contact angles.

4. Results & discussion

4.1. Printable domains

To investigate the effect of the electric field on the filament stability, we tested printing of 5 wt% aqueous PVA solution on the polyimide substrate under different EF strengths. A CCD camera was used to characterize the dynamic contact angles affected by the EF (Fig. 3). The advancing contact angle (θ_A') was captured when the liquid volume continues to grow with the pumping device and electric field activated. The equilibrium contact angle (θ_E') was captured when the liquid stabilizes with the pumping device shut down and the electric field still activated. At 0 kV/cm, the average advancing and equilibrium contact angles were 95° and 55°, respectively. At 5 kV/cm EF strength, the average advancing and equilibrium contact angles decreased to 60° and 48°, respectively. By further increasing the EF strength to 10 kV/cm, the angles dramatically decreased to 23° and 21°, respectively. Based on these measurements, the values of the coefficient C_E were established. The value of C_E decreased from 0.574 to 0.232 $s^{-2/3}$ when the EF strength increased from 0 to 10 kV/cm.

Afterward, straight filaments were printed using a 0.48 mm stainless steel dispensing nozzle at the 3 mm^3/s applied flow rate with the 9 mm/s printing speed. The thickness of the dielectric substrate was 0.3 mm, and the standoff distance was 0.5 mm. As demonstrated in Fig. 4, under 0 kV/cm (no EF), we observed periodic bulges on the printed filaments. Such periodicity can be explained by the capillary instability [28,29]. At the 5 kV/cm EF, the strength of the capillary instability was diminished, and the number of bulges significantly decreased. Furthermore, by increasing the EF strength to 10 kV/cm, no bulges were observed, validating the feasibility and effectiveness of EF as a remedy to the printing shape instability. In addition, our proposed electric-field-assisted approach is also feasible in layer-by-layer fabrication by adjusting the process parameters based on the layer thickness and material properties. For instance, when the first layer is thoroughly solidified via thermal curing, it adheres to the polyimide film and becomes a part of the dielectric layer. To print the remaining layers, one needs to increase the voltage to compensate for the slight increase in the dielectric layer thickness and the variation in the dielectric permittivity using Eq. (9) to maintain the consistent electrowetting effect. Also, it should be emphasized that because of the substrate change from

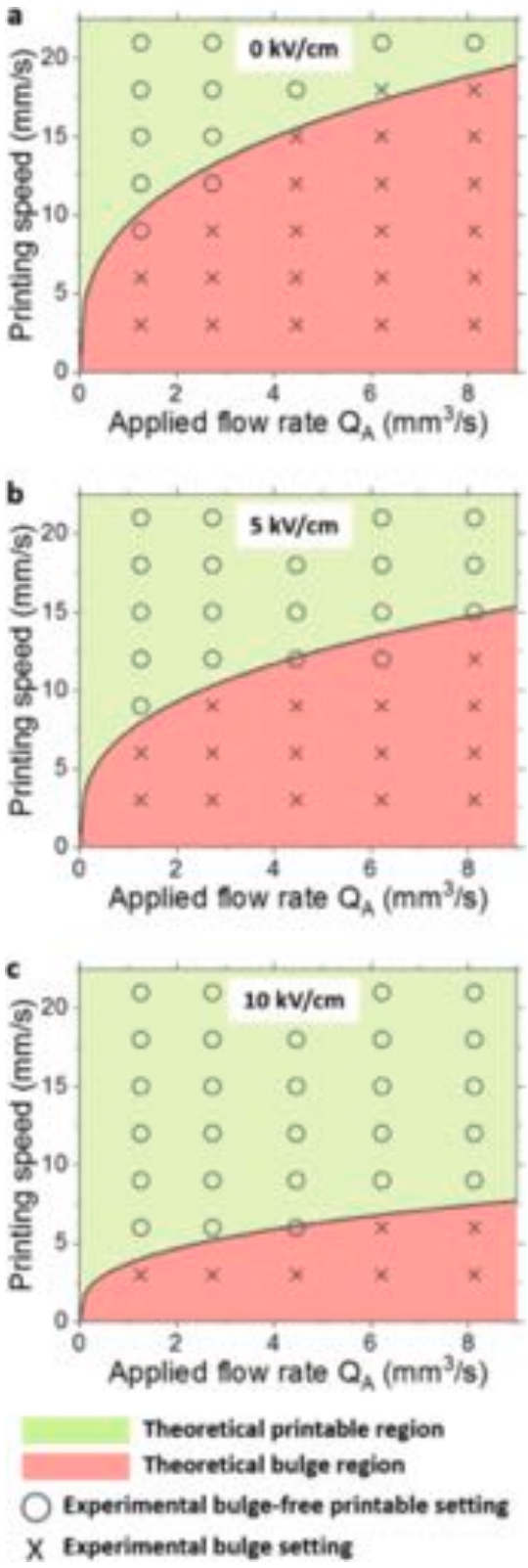

Fig. 5. Comparison of the theoretically predicted printable regions and the experimentally observed printable regions under different EF strengths. (a) 0 kV/cm. (b) 5 kV/cm. (c) 10 kV/cm.

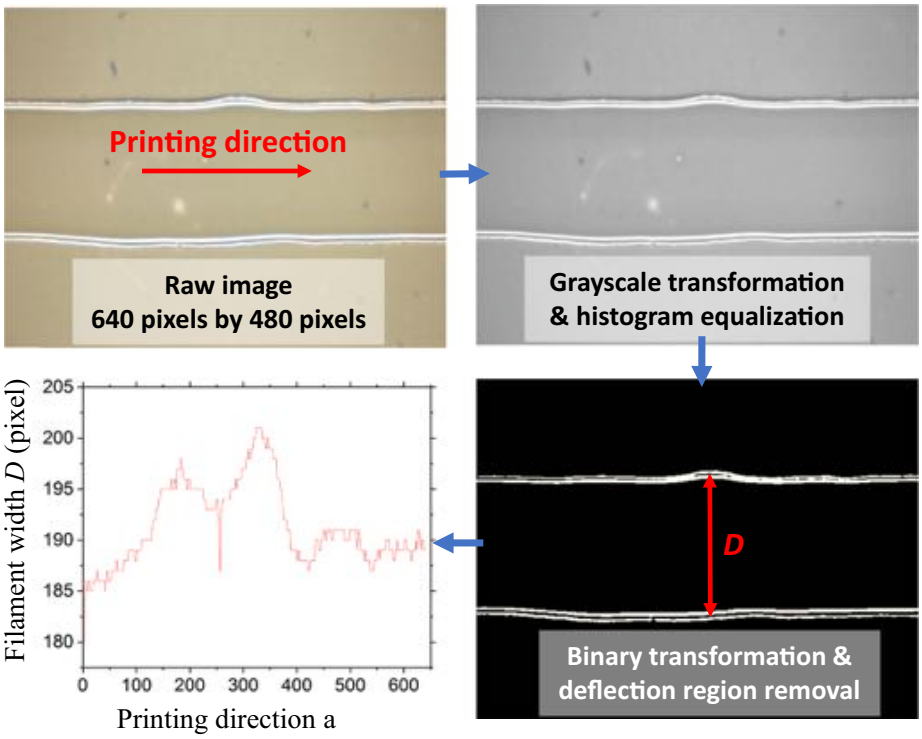

Fig. 6. Image processing method for geometrical accuracy analysis. (For interpretation of the references to color in this figure, the reader is referred to the web version of this article.)

polyimide to solidified PVA, the contact angles may differ, thus the applied flow rate should be updated using Eq. (4) to obtain an accurate filament width estimate to plan the process settings for printing a multi-layer structure.

Using the estimated values of C_E, we predicted the theoretical printable regions based on Eqs. (10)–(12). To experimentally validate the theoretically predicted printable regions, we tested more process parameter settings and examined whether there was any bulge formed on printed filaments. If no bulges were observed, the setting was identified as a bulge-free printable setting. Otherwise, the process setting was identified as a non-printable setting. As shown in Fig. 5, the circles marked DIW process settings that generated bulge-free printing results, while the crosses marked process settings that generated bulged filaments in the experiments. It is seen that the experimental boundaries between the domains (bulge-free settings) and the crosses domains (bulged settings) agree well with the theoretically predicted boundaries, validating the accuracy of the theoretical geometry model for the novel electric-field-assisted DIW process. Furthermore, the experimental results also validated the theoretical model prediction that electric-field significantly enlarges the bulge-free printable region of the 5 wt% PVA aqueous solution on polyimide substrate and increases the printing throughput. Such throughput enhancement is due to the reduced dynamic contact angle during printing, which led to a lower gradient of capillary pressure and the corresponding fluid flow along the printed filament. These findings not only verify the accuracy of the model predictions but also confirm the effectiveness of our proposed electric-field-assisted approach as a remedy to the bulge formation problem in DIW of low-viscosity liquids and a way of increasing the throughput.

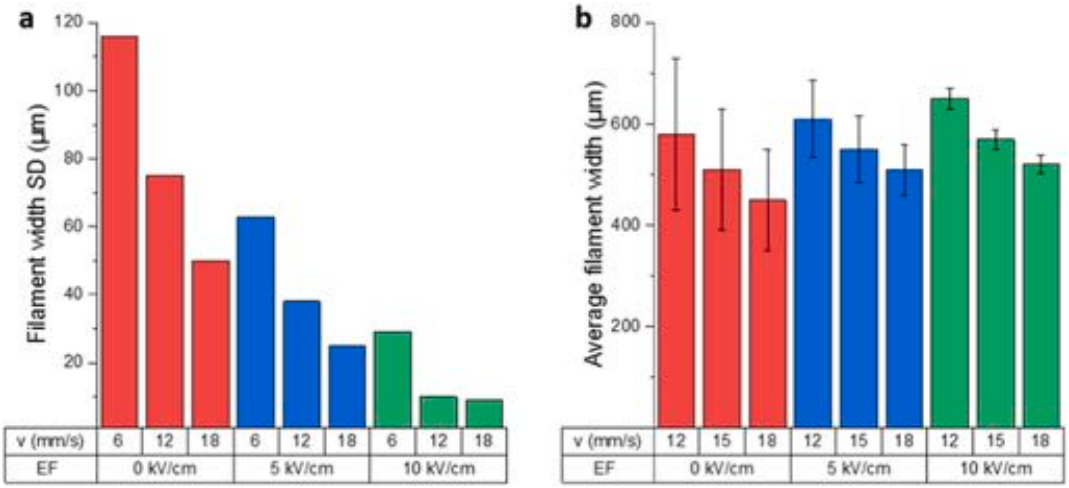

Fig. 7. Geometrical accuracy. (a) Standard deviation of the printed filament width under different EF strengths and printing speeds. (b) Expected width (mean) of the bulge-free filaments under different EF strengths and printing speeds: error bar is the 95% confidence interval.

4.2. Geometrical accuracy

To study the printing quality of the electric-field-assisted DIW process, we implemented an image processing approach to analyze statistically printed filaments. As shown in Fig. 6, the colored raw image of a printed filament (dimensions: 640 pixels by 480 pixels) was first obtained by a microscope (MicroVu Sol). The raw image was then transformed into a grayscale format, and a histogram equalization was conducted to pre-process the image to improve its contrast in MATLAB. The equalized grayscale image was further converted into the binary form and was processed using a median filter (kernel size: 5 to 15) to remove any undesirable light deflection region for the filament width measurement. The filament width at each location along the printing direction was measured by finding the filament boundary and subtracting the upper and lower bounds in MATLAB. The calculated data for each filament was transformed from pixel to physical size and stored as a vector with 640 elements for statistical analysis.

Using this image processing method, we analyzed the standard deviations of the width of filaments produced at 6, 12, and 18 mm/s printing speeds at the 3 mm^3/s applied flow rate under different EF strengths (Fig. 7a). It should be emphasized that some of these filaments corresponding to relatively slow printing speeds suffered from bulges. As expected, filaments formed under 0 kV/cm (without electric field) revealed the most visible waviness, with the standard deviation in width as high as 115 μm. After applying a 5 kV/cm EF strength, the corresponding standard deviation was reduced by approximately 40–60%. At the 10 kV/cm EF strengths, although filaments printed at 6 mm/s speed still revealed a moderate waviness (30 μm), the width deviation of filaments printed at higher speeds, such as 12 and 18 mm/s, is much smaller, down to 9 μm. Higher printing speeds and EF strengths enabled successful printing of bulge-free filaments with a consistent width. For those successfully printed filaments, the average width is shown in Fig. 7b and analyzed with a 95% confidence interval (CI). It revealed that although high printing speed alone was able to achieve a bulge-free filament printing, the within-filament width waviness was still large. With the application of EF, not only the bulge formation problem could be addressed, but also the within-filament width variation was reduced, thus enabling a more consistent printing result. In addition, when applying EF, the filament width was slightly increased by 10–20% due to the electric-field effect, and the increase was proportional to the EF strength. These experimental results validated the effectiveness of our novel method for improving the printed filament straightness, printing geometrical accuracy, and printing result consistency.

5. Conclusion

We introduced and investigated a novel electric-field-assisted direct ink writing process for defect-free printing using low-viscosity liquids. The electric field was applied between the dispensing nozzle and the substrate to overcome the fluid capillary instability in the printed filaments by decreasing the internal variation of the capillary pressure in the printing direction. A prediction model for the critical printing speed was developed and validated by test-printing a semi-dilute PVA aqueous solution on a polyimide substrate. Also, we implemented an image processing method to analyze the geometry of the printed filaments statistically. Compared with conventional DIW approaches, the proposed method significantly broadened the working window of process parameter settings and expanded the choice of inks with a >150% higher throughput. Our method also enhanced the printed filament's geometrical accuracy. The average straightness of printed filaments can be improved by more than 400%. The findings indicate potential importance of this electric-field-assisted method in production of future functional devices using relatively low-viscosity materials and the other applications.

In this study, a polyimide substrate was investigated owing to its excellent electrical insulation properties and wide applications in DIW. The surface energy of polyimide is approximately 50 mJ/m^2, which is relatively low among a variety of DIW substrates from metals to plastics. On substrates, which have an extremely low surface energy or a much higher surface energy than polyimide, electric fields may have very different influence on liquid flow dynamics under different process conditions. Future work is required to explore feasibility and effectiveness of the electric field in broadening the range of DIW-printable substrates in a wide surface energy range.

Declaration of competing interest

There is no conflict of interest.

Acknowledgements

This material is based upon work partially supported by the National Science Foundation under Grant No. 1825626.

References

[1] Rocha VG, Saiz E, Tirichenko IS, García-Tuñón E. Direct ink writing advances in multi-material structures for a sustainable future. J Mater Chem A 2020;8(31):15646–57.
[2] Kim Y, Yuk H, Zhao R, Chester SA, Zhao X. Printing ferromagnetic domains for untethered fast-transforming soft materials. Nature 2018;558(7709):274–9.
[3] Jiang Y, Cheng M, Shahbazian-Yassar R, Pan Y. Direct ink writing of wearable thermoresponsive supercapacitors with rGO/CNT composite electrodes. Adv. Mater. Technol. 2019;4(12):1900691.
[4] Noor N, Shapira A, Edri R, Gal I, Wertheim L, Dvir T. 3D printing of personalized thick and perfusable cardiac patches and hearts. Adv. Sci. 2019;6(11):1900344.
[5] Yang Y, Chen Z, Song X, Zhang Z, Zhang J, Shung KK, et al. Biomimetic anisotropic reinforcement architectures by electrically assisted nanocomposite 3D printing. Adv Mater 2017;29(11):1605750.
[6] Young AJ, Guillet-Nicolas R, Marshall ES, Kleitz F, Goodhand AJ, Glanville LB, et al. Direct ink writing of catalytically active UiO-66 polymer composites. Chem Commun 2019;55(15):2190–3.
[7] Cheng M, Ramasubramanian A, Rasul MG, Jiang Y, Yuan Y, Foroozan T, et al. Direct ink writing of polymer composite electrolytes with enhanced thermal conductivities. Adv Funct Mater 2020;31(4):2006683.
[8] Boley JW, White EL, Chiu GTC, Kramer RK. Direct writing of gallium-indium alloy for stretchable electronics. Adv Funct Mater 2014;24(23):3501–7.
[9] Skylar-Scott MA, Uzel SG, Nam LL, Ahrens JH, Truby RL, Damaraju S, et al. Biomanufacturing of organ-specific tissues with high cellular density and embedded vascular channels. Sci Adv 2019;5(9):eaaw2459.
[10] Gratson GM, Xu M, Lewis JA. Direct writing of three-dimensional webs. Nature 2004;428(6981):386.
[11] Smay JE, Cesarano J, Lewis JA. Colloidal inks for directed assembly of 3-D periodic structures. Langmuir 2002;18(14):5429–37.
[12] M'barki A, Bocquet L, Stevenson A. Linking rheology and printability for dense and strong ceramics by direct ink writing. Sci Rep 2017;7(1):1–10.
[13] Friedrich L, Begley M. In situ characterization of low-viscosity direct ink writing: stability, wetting, and rotational flows. J Colloid Interface Sci 2018;529:599–609.
[14] Skylar-Scott MA, Gunasekaran S, Lewis JA. Laser-assisted direct ink writing of planar and 3D metal architectures. Proc Natl Acad Sci 2016;113(22):6137–42.
[15] Zhou Z, Cantu LR, Chen X, Alexander MR, Roberts CJ, Hague R, et al. High-throughput characterization of fluid properties to predict droplet ejection for three-dimensional inkjet printing formulations. Addit Manuf 2019;29:100792.
[16] Barry III RA, Shepherd RF, Hanson JN, Nuzzo RG, Wiltzius P, Lewis JA. Direct-write assembly of 3D hydrogel scaffolds for guided cell growth. Adv Mater 2009;21(23):2407–10.
[17] Duineveld PC. The stability of ink-jet printed lines of liquid with zero receding contact angle on a homogeneous substrate. J Fluid Mech 2003;477:175–200.
[18] Stringer J, Derby B. Formation and stability of lines produced by inkjet printing. Langmuir 2010;26(12):10365–72.
[19] Jiang Y, Hu S, Pan Y. A normalized trace geometry modeling method with bulge-free analysis for direct ink writing process planning. 3D Print. Addit. Manuf. 2018;5(4):301–10.
[20] Quilliet C, Berge B. Electrowetting: a recent outbreak. Curr Opin Colloid Interface Sci 2001;6(1):34–9.
[21] Zhao YP, Wang Y. Fundamentals and applications of electrowetting. Rev. Adhesion Adhesives 2013;1(1):114–74.
[22] Mugele F, Baret JC. Electrowetting: from basics to applications. J Phys Condens Matter 2005;17(28):R705.
[23] Watson AM, Cook AB, Tabor CE. Electrowetting-assisted selective printing of liquid metal. Adv Eng Mater 2019;21(10):1900397.
[24] Plog J, Löwe JM, Jiang Y, Pan Y, Yarin AL. Control of direct written ink droplets using electrowetting. Langmuir 2019;35(34):11023–36.
[25] Li X, Tian H, Wang C, Li X, Shao J, Ding Y, et al. Electrowetting assisted air detrapping in transfer micromolding for difficult-to-mold microstructures. ACS Appl Mater Interfaces 2014;6(15):12737–43.

[26] Kang KH. How electrostatic fields change contact angle in electrowetting. Langmuir 2002;18(26):10318–22.
[27] Bateni A, Laughton S, Tavana H, Susnar SS, Amirfazli A, Neumann AW. Effect of electric fields on contact angle and surface tension of drops. J Colloid Interface Sci 2005;283(1):215–22.
[28] Sekimot K, Oguma R, Kawasaki K. Morphological stability analysis of partial wetting. Ann Phys Rehabil Med 1987;176(2):359–92.
[29] Schiaffino S, Sonin AA. Formation and stability of liquid and molten beads on a solid surface. J Fluid Mech 1997;343:95–110.